Unveiling the effect of Ni on the formation and structure of Earth's inner core

Yang Sun[a,b,c,1] [ID], Mikhail I. Mendelev[c,1] [ID], Feng Zhang[c], Xun Liu[d], Bo Da[d], Cai-Zhuang Wang[c], Renata M. Wentzcovitch[b,e,f,g,h,1] [ID], and Kai-Ming Ho[c]

Ni is the second most abundant element in the Earth's core. Yet, its effects on the inner core's structure and formation process are usually disregarded because of its electronic and size similarity with Fe. Using ab initio molecular dynamics simulations, we find that the bcc phase can spontaneously crystallize in liquid Ni at temperatures above Fe's melting point at inner core pressures. The melting temperature of Ni is shown to be 700 to 800 K higher than that of Fe at 323 to 360 GPa. hcp, bcc, and liquid phase relations differ for Fe and Ni. Ni can be a bcc stabilizer for Fe at high temperatures and inner core pressures. A small amount of Ni can accelerate Fe's crystallization at core pressures. These results suggest that Ni may substantially impact the structure and formation process of the solid inner core.

Earth's inner core | solidification | supercooling | atomistic simulation | iron alloy

The Earth has a liquid outer core and a solid inner core composed of FeNi alloy and light elements (1–3). The crystal structure(s) in the solid inner core is fundamental for understanding the inner core formation and its seismological properties, but its crystalline phase(s) is still under debate. The Fe alloys in the inner core are often believed to have the hexagonal close-packed (hcp) lattice (4, 5), but the body-centered cubic (bcc) phase remains under consideration (6, 7). Thermodynamic calculations indicate that hcp Fe is the stable solid phase at inner core pressures. Still, the Gibbs free energy difference between the hcp and bcc phases can be quite small near the melting points of these Fe phases at inner core pressures (8–10), which is on the order of tens of meV/atom (10), a value close to the thermal energy per atom at room temperature.

The presence of other elements diluted in Fe can further change the stability fields of crystalline phases (11, 12). Cosmochemical and geochemical models estimated 5 to 15 wt% Ni content in the Earth's core (1, 13). Ni is known to stabilize the fcc phase with respect to hcp under low $P–T$ conditions (14–17). The bcc phase was once reported in a $Fe_{90}Ni_{10}$ alloy by experiments at pressures above 225 GPa and temperatures over 3,400 K (18). However, later experiments did not confirm the existence of the bcc phase in $Fe_{90}Ni_{10}$ (19, 20). Ab initio calculations demonstrated that Ni doping could improve the dynamic stability of bcc Fe (21). The coexistence of hcp and an ordered binary bcc phase (B2) was observed when sufficient Si was mixed with Fe or FeNi alloys at ~200 GPa (22, 23). This suggests the possibility of hcp-bcc coexistence in the inner core, though much more evidence is needed to confirm it.

The growth of the present solid core provides the primary power source to sustain the outer core convection, which generates the Earth's magnetic field (24). Despite its importance, significant gaps exist in understanding the inner core's age and nucleation process (25–28). Recent simulations showed that the hcp nucleation requires much larger supercooling than the liquid core can reach, leading to the "inner core nucleation paradox" (29–32). In pure Fe, the metastable bcc phase was shown to nucleate at smaller supercooling than the hcp phase under the core's condition, which is a two-step nucleation process that may help resolve the paradox (32). While the study of Ni and FeNi melting temperatures at 120 GPa (33–35) suggested that Ni could strongly modify the triple point in a $Fe_{1-x}Ni_x$ alloy (35), the effect of Ni on the inner core nucleation process is yet to be considered.

Previous ab initio quasiharmonic calculations of Ni and Fe–Ni alloys at Earth's core pressures focused mainly on the fcc–hcp phase relation and assumed anharmonicity to be negligible (19). However, the solid inner and liquid outer core coexist at the inner core boundary (ICB) close to the melting point. Anharmonic effects can significantly affect the free energies and phase stabilities, especially in the bcc phase (32, 36, 37). One practical way to determine the stable phase near the melting point is to compute the melting temperatures of competing crystalline phases when the stable solid phase is uncertain. These melting temperatures define the relative stability of different solid phases for liquid coexistence: the phase with the highest melting temperature is the most stable, while other

Significance

The Earth's inner core growth is a key process for understanding Earth's evolution. This process is inherently related to the crystallization properties of the core's constituents, primarily Fe, Ni, and some light elements. This work demonstrates that the core's second most abundant element, Ni, strongly affects Fe's crystallization process. Ni can stabilize the bcc phase and accelerate Fe's crystallization under core pressures. The simulation results suggest that alloying Fe with Ni can promote the coexistence of the bcc and hcp phases in the solid inner core. This is critical in understanding the inner core's nucleation and the origin of its complex solid structure.

crystalline phases are metastable. In this work, we start with an unexpected simulation result, i.e., the crystallization of liquid Ni at ICB conditions. Then, we address Ni's hcp, fcc, and bcc phase stability near the melting temperature and compare it with the corresponding data for Fe. Combining crystallization kinetics and free-energy results of FeNi systems, we discuss possible scenarios for the effect of Ni on the formation and structure of the inner core.

Results and Discussion

Bcc Crystallization. Our ab initio calculations showed that the melting temperature of hcp Fe is 5,848 ±15 K at 323 GPa (10), consistent with previous calculations of 5,730 ± 200 K using the same pseudopotentials (38). Including more valence electrons in the pseudopotential systematically increases the melting points but does not significantly change the relative stability between the hcp and bcc phases (10) (*Methods*). If Ni were similar to Fe, as usually assumed, one would expect a similar melting temperature for Ni at the same pressures. Surprisingly, liquid Ni spontaneously crystallizes in an ab initio molecular dynamics (AIMD) simulation at 6,000 K and 323 GPa, well above Fe's melting point. Fig. 1*A* shows the enthalpy change as a function of time during an AIMD simulation. The sharp drop of the enthalpy at ~30 ps indicates a clear first-order phase transition. Fig. 1*B* shows that the fraction of the bcc phase quickly increases at ~30 ps, which coincides with the enthalpy change in Fig. 1*A*. The fraction of hcp also increases at 30 ps and stays steady at 31 ps but quickly decreases after the bcc phase becomes dominant. The fraction of fcc during the crystallization is insignificant. The phase competition is mainly between hcp and bcc during the nucleation process. The initial and final snapshots in Fig. 1*C* confirm that the liquid solidified into the bcc phase during the AIMD simulation. The unexpected solidification in the simulation suggests that Ni should have a

much higher melting temperature than Fe. The crystallization of the bcc phase also indicates that bcc is dynamically stabilized by anharmonic fluctuations at 6,000 K, despite being an unstable phase at 0 K (39).

Crystallization is a rare event challenging to observe spontaneously in simulations. Classical nucleation theory (40) establishes that the nucleation rate depends exponentially on the nucleation barrier ΔG^*, as $J = \kappa \cdot \exp\left(-\frac{\Delta G^*}{k_B T}\right)$, where κ is a kinetic prefactor. The fast crystallization observed here indicates a significantly large nucleation rate, thus a small nucleation barrier. The key factors determining the nucleation barrier ΔG^* are the free energy difference between the bulk solid and liquid phase and the solid–liquid interface (SLI) free energy. While the bcc phase prevails over hcp in the crystallization process, it does not necessarily mean that bcc Ni has significantly lower free energy than hcp Ni. In the case of Fe, *metastable* bcc can have a nucleation rate 10 to 40 orders of magnitude higher than that of the stable hcp phase at 1,000 to 600 K supercooling (32), because the SLI free energy for Fe's bcc phase is much smaller than that for the hcp phase (32). Therefore, one needs the free energy relations to determine the relative thermodynamic stability of bcc, hcp, and liquid for Ni. As free energy relations also define melting relations, we use the latter to infer thermodynamic stability among these phases.

Phase Relations Near the Melting Temperature. We recently showed that the melting temperature could be accurately obtained from ab initio simulations with the help of a semiempirical potential if the potential provides atomic structures close to those obtained in the AIMD simulation (10). Therefore, we developed a Finnis–Sinclair (FS) type potential (41) for Ni in the present study. *SI Appendix* contains details of potential and accuracy tests. The bcc, hcp, and fcc melting temperatures for this FS potential are computed by two-phase coexistence
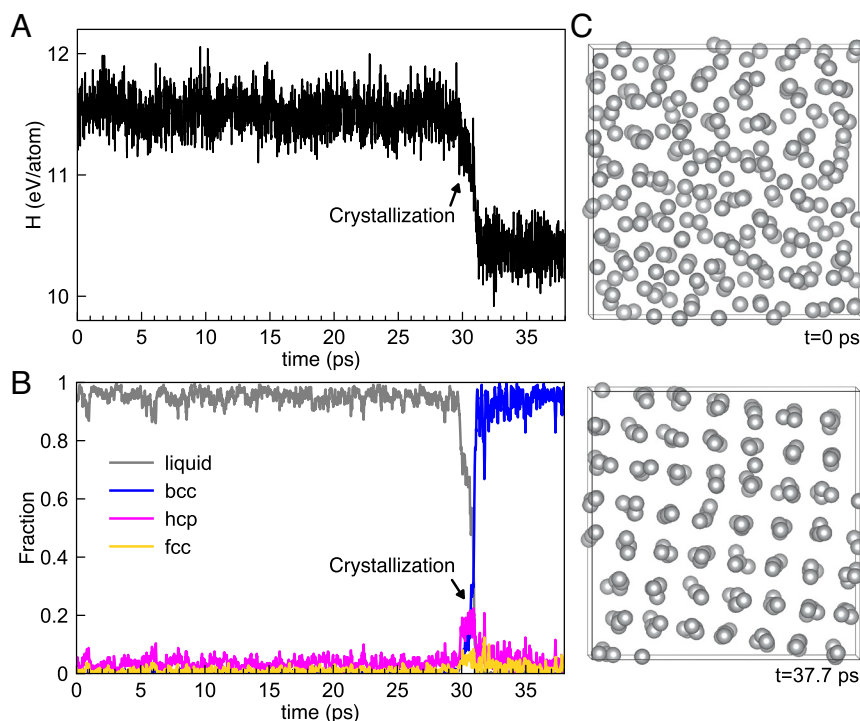

Fig. 1. Crystallization from liquid to bcc at 323 GPa and 6,000 K by the AIMD simulation. (*A*) Enthalpy as a function of simulation time. The arrow marks the crystallization. (*B*) The fraction of liquid and crystalline atoms as a function of simulation time. The arrow marks the crystallization. (*C*) Initial (*Upper*) and final (*Bottom*) atomic configuration snapshot in a supercell with 250 atoms.

Table 1. Melting temperatures of Fe and Ni phases at 323 and 360 GPa obtained from ab initio calculations

System	P (GPa)	T_m^{bcc} (K)	T_m^{hcp} (K)	T_m^{fcc} (K)
Ni	323	6,528	6,499	6,492
Ni	360	6,870	6,833	6,824
Fe	323	5,632	5,848	–
Fe	360	5,850	6,094	–

Fe data are taken from ref. 10, The uncertainty is 15 K.

simulations with large-scale classical MD. While no information about the melting temperatures was included in the potential development, the FS potential predicts that bcc-Ni has the highest melting temperature. We calculated the ab initio free energy via thermodynamic integration (TI), using the classical system described by the FS potential as the reference state. Table 1 shows the ab initio melting temperatures of the three phases computed at 323 and 360 GPa, which are the pressures at the boundary and center of the inner core, respectively. Bcc-Ni indeed shows higher melting temperatures than hcp-Ni and fcc-Ni. The differences are small, ~30 K, but are more significant than the typical confidence interval of 15 K in similar calculations (10). The difference between hcp-Ni and fcc-Ni melting temperatures is smaller, ~7 K. In Table 1, we compare the melting temperatures of Ni phases to those of Fe phases computed in ref. 10. Both bcc and hcp Ni's melting temperatures are significantly higher than those for Fe phases by 700 to 800 K.

Fig. 2A shows the relative free energy difference referenced to the bcc phase at 323 GPa. For Ni, bcc is the stable phase from 6,528 to 6,366 K. At temperatures lower than 6,366 K, hcp becomes the stable phase while bcc becomes metastable. A comparison between Fig. 2 A and B shows that the bcc–hcp phase relations are very different between Fe and Ni systems. The bcc phase is always metastable for Fe, while it is stable for Ni in a small temperature range near the melting point. The free energy difference between hcp and bcc is much smaller for Ni than for Fe. Therefore, Ni is likely a bcc stabilizer if mixed with Fe at high temperatures under core pressures.

Crystallization of Fe–Ni Mixture. The comparisons between pure Fe and Ni suggest that the effect of Ni on the core's structure and formation should be carefully considered. Previous studies have found that liquid Fe at core pressures requires an unrealistically large undercooling to nucleate the solid inner core phase, which is unlikely to be reached under Earth's core conditions and age (29, 31, 32). Bcc nucleation in the pure Fe phase can reduce the nucleation barrier of hcp, even though this mechanism cannot fully resolve the nucleation paradox yet (32). Since the bcc phase is the stable high-temperature phase of Ni, mixing Ni in Fe might provide another mechanism to accelerate the nucleation process. We performed AIMD simulations of pure Fe and $Fe_{85}Ni_{15}$ liquids at large supercooling temperatures under core pressures to examine this scenario. At ~310 GPa and 5,000 K, the $Fe_{85}Ni_{15}$ liquid crystallizes within 50 ps, as shown in Fig. 3A. In contrast, no crystallization was observed for the pure Fe liquid up to 76 ps under the same P–T condition. Crystallization is a stochastic process; consequently, the nucleation incubation time can fluctuate. To explore this stochastic effect, we performed three additional AIMD simulations for $Fe_{85}Ni_{15}$ and pure Fe. The results are presented in *SI Appendix*, Fig. S3. We found the averaged crystallization time for $Fe_{85}Ni_{15}$ is ~40 ps, while no crystallization can be observed
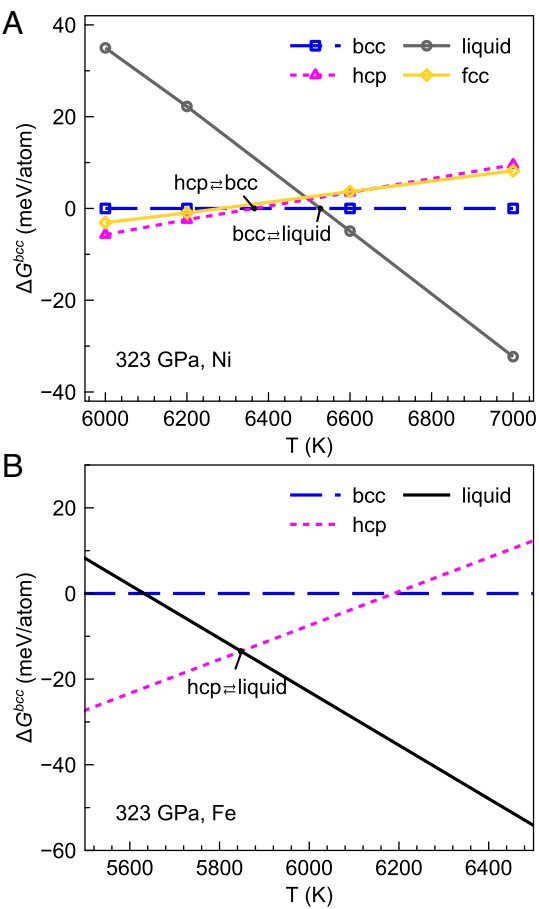
Fig. 2. Ab initio free energy difference referenced to the bcc phase at 323 GPa near the melting temperatures for Ni and Fe. (*A*) The open circles are obtained through TI calculations. The circles are connected to guide the eyes. The two black dots at 6,366 and 6,528 K indicate hcp–bcc and bcc–liquid phase transitions, respectively. (*B*) The free energy data of Fe are from ref. 10. The black dot indicates the phase transition of hcp–liquid. The uncertainty is ~1 meV/atom due to the size effect (10).

with pure Fe up to 80 ps at 5,000 K and 310 GPa. This suggests that the $Fe_{85}Ni_{15}$ alloy has a higher nucleation rate than pure Fe at the same temperature. While the AIMD is limited by simulation size, Ni's effect on accelerating Fe's crystallization process can also be observed from large-scale classical MD simulations by cooling the melts with ultrahigh cooling rates (*SI Appendix*, Note 2). Then, 15% Ni reduces the required supercooling by ~400 K under a simulation cooling rate of 10^{11} K/s. While this cooling rate is far from Earth's core condition, it validates Ni's effect on Fe's crystallization revealed by the AIMD simulations.

The crystallization process of $Fe_{85}Ni_{15}$ liquid in the AIMD simulations is analyzed based on its local atomic structure change shown in Fig. 3B. The liquid shows two attempts to nucleate: first at ~25 ps, then at 47 ps. In the first attempt, an hcp nucleus emerges but only grows to a small size and then remelts. This indicates that the nucleus cannot overcome the nucleation barrier to reach the critical size. In the second attempt, a bcc nucleus emerges and successfully crystallizes. During the bcc growth, ~20% of liquid atoms transform to hcp. It forms a bcc–hcp coexisting system in the as-crystallized solid, shown in Fig. 3C. The partial pair correlation functions of Fe and Ni are almost indistinguishable, suggesting Fe and Ni atoms randomly distribute in the as-crystallized solid. This is consistent with previous calculations that Fe and Ni do not form stoichiometric compounds but
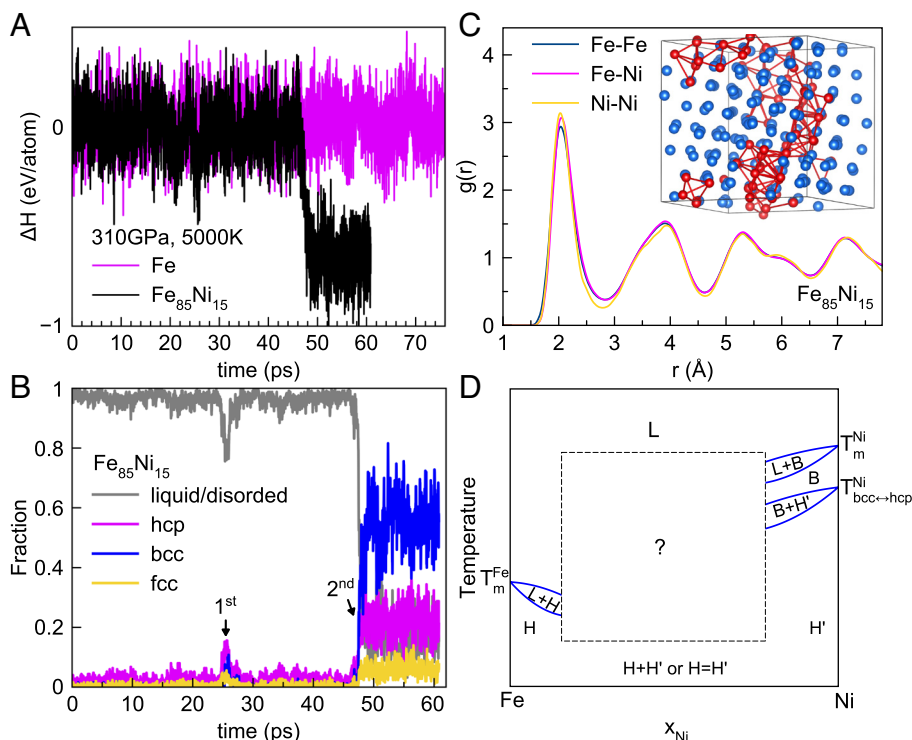
Fig. 3. Fe and $Fe_{85}Ni_{15}$ liquid at 310 GPa and 5,000 K from AIMD simulation. (*A*) The enthalpy change as a function of simulation time. The data are referenced to averaged liquid enthalpy for Fe and $Fe_{85}Ni_{15}$, respectively. (*B*) The fraction of liquid/disordered and crystalline atoms as a function of time in $Fe_{85}Ni_{15}$ simulation. The arrows mark the two nucleation attempts. (*C*) The partial pair correlation function of the crystallized $Fe_{85}Ni_{15}$ phase averaged over the last 10 ps of the simulation. The insert shows the final atomic configuration. The center atoms of hcp-like clusters are colored red and connected to guide the eyes. Blue are bcc. (*D*) Schematic of a "likely" Fe–Ni liquid-bcc–hcp phase diagram. Ni (T_m^{Ni}) has a higher melting temperature than Fe (T_m^{Fe}). For pure Fe, hcp is the stable phase, and bcc is metastable. For pure Ni, bcc is the high-tempeature stable phase and transform to hcp at lower temperatures. L stands for liquid phase; B is bcc phase and H and H′ are hcp phases. Dashed box indicates uncertain shape/existence. H+H′ indicates the potential existence of two hcp solid solutions with different compositional fields, while H=H′ indicates a single hcp solid solution.

only completely disordered solid solutions under core conditions (42, 43). Additional three AIMD simulations of $Fe_{85}Ni_{15}$ crystallization in *SI Appendix*, Fig. S3 also show minor hcp phases in the as-crystallized bcc phases.

Discussion

The current results demonstrate that Ni strongly stabilizes the bcc phase and accelerates the crystallization of Fe under Earth's core conditions. Moreover, our simulation showed that bcc and hcp can coexist during the crystallization of $Fe_{85}Ni_{15}$ alloy. These results suggest a potential coexistence of hcp and bcc phases under Earth's inner core. Using this study's minimal free energy data, one can propose a binary Fe–Ni phase diagram, as illustrated in Fig. 3*D*. On the Ni side, the bcc phase has a stability field close to the melting curve. This bcc stability field can extend into the Fe-rich domain, posing a challenge to the stability of hcp, potentially leading to the emergence of a liquid–hcp–bcc eutectic. Thus, there's a possibility for a thermodynamically stable coexistence of bcc and hcp in the solid phase of the inner core. At lower temperatures, when both Fe and Ni are in the hcp phase, they might form two distinct hcp phases (H+H′) with varying Ni compositions or a solid solution, depending on how different or similar their partial molar volumes are. To solve the unknown region of the phase diagram in Fig. 3*D*, one needs to compute the free energy of liquid, hcp, and bcc phases as a function of Ni content under the Earth's core conditions, where anharmonicity and configurational entropy contributions need to be carefully treated.

Our results in Fig. 2 suggest that pure Ni bcc is only stable in a narrow ~150 K temperature range below the melting

temperature. Below this temperature, it becomes hcp or fcc. In pure Fe, bcc is metastable with a higher nucleation rate than the hcp phase. It is a metastable transient phase between the liquid and the hcp phases (32). It might be difficult to observe even near the melting temperature. Together, these observations suggest the stability field of the bcc FeNi alloy should lie at very high temperatures, close to the liquidus line. This may explain the failure to observe bcc phases in previous experiments (19, 20) as the temperatures were not high enough to reach bcc's stability field. Interestingly, while bcc phase was not observed in $Fe_{90}Ni_{10}$ at 2,730 K and 250 GPa (19), the same group of authors recently reported the coexistence of hcp and B2 phases in the $Fe_{93}Ni_7$ alloy at 2,970 K and 186 GPa (23). To fully resolve the controversy, the nature of the equilibrium states of $Fe_{1-x}Ni_x$ alloy in Fig. 3*D* should be investigated via simulations and experiments in future studies. If the bcc phase indeed exists in the inner core, its different density and seismological properties with respect to the hcp phase should be considered when constraining the light elements composition in the outer and inner core (3). The coexistence of bcc and hcp phases may result in stratification or other non-random phase distribution in the inner core (44). For instance, the inner core should have been Ni-rich in its youth, a situation that should still persist today owing to continuous early Ni depletion from the melt. Besides, the higher melting temperature of Ni implies that the inner core should have nucleated earlier than estimations based solely on pure Fe suggest. A comprehensive Fe–Ni phase diagram encompassing liquidus, solidus, and solvus curves is essential to advance understanding of the Earth's inner core composition, structure, and the associated wave speed heterogeneities (45, 46).

To conclude, we find that the bcc phase crystallizes from Ni liquid at a temperature above the melting point of Fe under inner core pressures. Ab initio free energy calculations indicate that Ni's melting temperature is ~700 to 800 K higher than Fe's at 323 to 360 GPa. Bcc is the thermodynamically stable phase near Ni's melting point at inner core pressures. Ni accelerates Fe's crystallization process at inner core conditions. The Fe–Ni mixture may lead to the coexistence of hcp and bcc phases under core conditions. These results suggest that Ni can be a key factor in modeling the Earth's inner core formation and present structure.

Methods

AIMD Simulations. AIMD was employed with the Born Oppenheimer approach to simulate crystallization, collect input data to develop a semi-empirical potential, and perform TI calculations. The Vienna ab initio simulation package (VASP) (47) was employed for the density-functional theory (DFT) calculations. The projected augmented-wave (PAW) potentials shipped with VASP were used to describe the electron-ion interaction with 8 and 10 valence electrons for Fe and Ni, respectively. The core radii cutoff of these PAW potential is 1.2 Å. The effect of the number of valence electrons was examined in the calculation of the Fe's melting temperature of the bcc and hcp phases (10). At 323 GPa, Fe hcp and bcc's melting temperatures are 5,848 and 5,632 K, respectively, with PAW8 potential. They are 6,357 and 6,168 K with PAW16 potential, which includes additional $3s^23p^6$ electrons. The difference between hcp and bcc T_m was 216 and 189 K for PAW8 and PAW16 potentials, respectively. Therefore, including more inner shell electrons as valence electrons can systematically increase the melting temperature (10, 38). However, it does not significantly affect the relative melting temperature differences between the bcc and hcp phases (10). To achieve sufficiently long simulations of crystallization, we employ the PAW potentials without $3s^23p^6$ for both Fe and Ni. The generalized gradient approximation (GGA) in the Perdew–Burke–Ernzerhof (PBE) form was employed for the exchange-correlation energy functional. A plane-wave basis set was used with a kinetic energy cutoff of 400 eV. The AIMD simulations were performed for the constant number of atoms, volume, and temperature (NVT) canonical ensemble. Ni and $Fe_{85}Ni_{15}$ liquids are modeled in the crystallization simulations by 250 Ni atoms and $Fe_{212}Ni_{38}$ atoms, respectively. The Γ point was used to sample the Brillouin zone of these supercells. A time step of 1.5 fs was used to integrate Newton's equations of motion. The Nosé–Hoover thermostat was employed to control the temperature. The electronic entropy at high temperatures was described by the Mermin functional (48, 49). The non-magnetic calculations were performed in AIMD. We tested the spin-polarized calculations and found that the magnetic moments of the Fe and Ni phases are quenched when the electronic temperature is more than 4,000 K at 323 GPa.

Local Structure Characterization. The cluster alignment (CA) method (50, 51) was employed to recognize bcc, fcc, and hcp short-range orders in the local atomic clusters during crystallization. The CA method aligns the atomic clusters to the standard bcc, fcc, and hcp templates and computes the RMSD between the atomic clusters and templates. *SI Appendix*, Fig. S4 indicates that CA can distinguish well crystalline phases from the liquid. To remove the noise caused by thermal fluctuations, the atomic positions were averaged for 0.06 ps to perform the CA analysis.

Classical Molecular Dynamics Simulations. Classical molecular dynamics (CMD) simulations were performed with LAMMPS (large-scale atomic/molecular massively parallel simulator) code (52). The interatomic interaction was modeled using the FS type (41) semi-empirical potential developed in this work. During the MD simulation, the constant number of atoms, pressure, and temperature (NPT) ensemble was applied with the Nosé–Hoover thermostat and barostat. The time step of the simulation was 1.0 fs. The melting temperatures of the classical system, denoted as T_C^m, were determined using the solid–liquid coexistence approach (53) with 22,500 atoms. The free energy difference between liquid and solid, ΔG_C^{L-S}, is determined by the Gibbs–Helmholtz equation,

$$\Delta G_C^{L-S}(T) = -T\int_{T_C^m}^{T}\frac{\Delta H(T)}{T^2}dT,\qquad [1]$$

where ΔH is the latent heat computed by the enthalpy difference between liquid and solid from classical simulations with 5,000 atoms.

Ab Initio Melting Temperature. The ab initio melting temperature, $T_\mathcal{A}^m$, was obtained when the ab initio free energy difference between liquid and solid phases is zero, i.e., $\Delta G_\mathcal{A}^{L-S}(T_\mathcal{A}^m) = 0$. $\Delta G_\mathcal{A}^{L-S}$ is computed by TI between the classical system (C) and ab initio system ($\mathcal{A}$) (10). It was performed by exchanging the ab initio and classical atomic information on-the-fly in an MD simulation (10). CMD simulations were performed with LAMMPS (large-scale atomic/molecular massively parallel simulator) code (52). The NVT ensemble was applied during the TI-MD, and the Nosé–Hoover thermostat (54) was employed to control the temperature. A time step of 2.0 fs was used to integrate Newton's equations of motion. Supercells with 288, 256, 250, and 250 atoms were used to simulate hcp, fcc, bcc, and liquid, respectively.

Data, Materials, and Software Availability. All study data are included in the article and/or *SI Appendix*.

Author affiliations: ªDepartment of Physics, Xiamen University, Xiamen 361005, China; ᵇDepartment of Applied Physics and Applied Mathematics, Columbia University, New York, NY 10027; ᶜDepartment of Physics, Iowa State University, Ames, IA 50011; ᵈCenter for Basic Research on Materials, National Institute for Materials Science, Ibaraki 305-0044, Japan; ᵉDepartment of Earth and Environmental Sciences, Columbia University, New York, NY 10027; ᶠLamont–Doherty Earth Observatory, Columbia University, Palisades, NY 10964; ᵍData Science Institute, Columbia University, New York, NY 10027; and ʰCenter for Computational Quantum Physics, Flatiron Institute, New York, NY 10010

1. F. Birch, Elasticity and constitution of the Earth's interior. *J. Geophys. Res.* **57**, 227–286 (1952).
2. K. Hirose, S. Labrosse, J. Hernlund, Composition and state of the core. *Annu. Rev. Earth Planet Sci.* **41**, 657–691 (2013).
3. K. Hirose, B. Wood, L. Vočadlo, Light elements in the Earth's core. *Nat. Rev. Earth Environ.* **2**, 645–658 (2021).
4. O. L. Anderson, Properties of iron at the Earth's core conditions. *Geophys. J. Int.* **84**, 561–579 (1986).
5. G. Steinle-Neumann, L. Stixrude, R. E. Cohen, O. Gülseren, Elasticity of iron at the temperature of the Earth's inner core. *Nature* **413**, 57–60 (2001).
6. L. Vočadlo et al., The stability of bcc-Fe at high pressures and temperatures with respect to tetragonal strain. *Phys. Earth Planet. Inter.* **170**, 52–59 (2008).
7. A. B. Belonoshko, S. I. Simak, W. Olovsson, OYu. Vekilova, Elastic properties of body-centered cubic iron in Earth's inner core. *Phys. Rev. B* **105**, L180102 (2022).
8. L. Stixrude, Structure of Iron to 1 Gbar and 40,000 K. *Phys. Rev. Lett.* **108**, 055505 (2012).
9. J. Bouchet, S. Mazevet, G. Morard, F. Guyot, R. Musella, Ab initio equation of state of iron up to 1500 GPa. *Phys. Rev. B* **87**, 094102 (2013).
10. Y. Sun et al., Ab Initio melting temperatures of bcc and hcp iron under the Earth's inner core condition. *Geophys. Res. Lett.* **50**, e2022GL102447 (2023).
11. L. Vočadlo et al., Possible thermal and chemical stabilization of body-centred-cubic iron in the Earth's core. *Nature* **424**, 536–539 (2003).
12. A. S. Côté, L. Vočadlo, J. P. Brodholt, Light elements in the core: Effects of impurities on the phase diagram of iron. *Geophys. Res. Lett.* **35**, L05306 (2008).
13. V. F. Buchwald, *Handbook of Iron Meteorites: Their History, Distribution, Composition and Structure* (Center for Meteorite Studies, Arizona State University, 1975).
14. J. Lin et al., Iron-nickel alloy in the Earth's core. *Geophys. Res. Lett.* **29**, 109-1–109-3 (2002).

15. W. L. Mao, A. J. Campbell, D. L. Heinz, G. Shen, Phase relations of Fe–Ni alloys at high pressure and temperature. *Phys. Earth Planet. Inter.* **155**, 146–151 (2006).
16. T. Komabayashi, K. Hirose, Y. Ohishi, In situ X-ray diffraction measurements of the fcc-hcp phase transition boundary of an Fe-Ni alloy in an internally heated diamond anvil cell. *Phys. Chem. Miner.* **39**, 329–338 (2012).
17. T. Komabayashi, Phase relations of Earth's core-forming materials. *Crystals (Basel)* **11**, 581 (2021).
18. L. Dubrovinsky et al., Body-centered cubic iron-nickel alloy in Earth's core. *Science* **316**, 1880–1883 (2007).
19. T. Sakai, E. Ohtani, N. Hirao, Y. Ohishi, Stability field of the hcp-structure for Fe, Fe-Ni, and Fe–Ni–Si alloys up to 3 Mbar. *Geophys. Res. Lett.* **38**, 2–6 (2011).
20. S. Tateno, K. Hirose, T. Komabayashi, H. Ozawa, Y. Ohishi, The structure of Fe-Ni alloy in Earth's inner core. *Geophys. Res. Lett.* **39**, 2–5 (2012).
21. S. Chatterjee, S. Ghosh, T. Saha-Dasgupta, Ni doping: A viable route to make body-centered-cubic Fe stable at Earth's inner core. *Minerals* **11**, 1–12 (2021).
22. R. A. Fischer et al., Phase relations in the Fe-FeSi system at high pressures and temperatures. *Earth Planet. Sci. Lett.* **373**, 54–64 (2013).
23. D. Ikuta, E. Ohtani, N. Hirao, Two-phase mixture of iron–nickel–silicon alloys in the Earth's inner core. *Commun. Earth Environ.* **2**, 225 (2021).
24. J. R. Lister, B. A. Buffett, The strength and efficiency of thermal and compositional convection in the geodynamo. *Phys. Earth Planet. Inter.* **91**, 17–30 (1995).
25. K. Ohta, Y. Kuwayama, K. Hirose, K. Shimizu, Y. Ohishi, Experimental determination of the electrical resistivity of iron at Earth's core conditions. *Nature* **534**, 95–98 (2016).
26. Z. Konôpková, R. S. McWilliams, N. Gómez-Pérez, A. F. Goncharov, Direct measurement of thermal conductivity in solid iron at planetary core conditions. *Nature* **534**, 99–101 (2016).
27. A. J. Biggin et al., Palaeomagnetic field intensity variations suggest Mesoproterozoic inner-core nucleation. *Nature* **526**, 245–248 (2015).
28. T. Zhou et al., Early Cambrian renewal of the geodynamo and the origin of inner core structure. *Nat. Commun.* **13**, 1–7 (2022).
29. L. Huguet, J. A. Van Orman, S. A. Hauck, M. A. Willard, Earth's inner core nucleation paradox. *Earth Planet. Sci. Lett.* **487**, 9–20 (2018).
30. C. J. Davies, M. Pozzo, D. Alfè, Assessing the inner core nucleation paradox with atomic-scale simulations. *Earth Planet. Sci. Lett.* **507**, 1–9 (2019).
31. A. J. Wilson, A. M. Walker, D. Alfè, C. J. Davies, Probing the nucleation of iron in Earth's core using molecular dynamics simulations of supercooled liquids. *Phys. Rev. B* **103**, 214113 (2021).
32. Y. Sun, F. Zhang, M. I. Mendelev, R. M. Wentzcovitch, K.-M. Ho, Two-step nucleation of the Earth's inner core. *Proc. Natl. Acad. Sci. U.S.A.* **119**, e2113059119 (2022).
33. O. T. Lord et al., The melting curve of Ni to 1 Mbar. *Earth Planet. Sci. Lett.* **408**, 226–236 (2014).
34. S. Boccato et al., The melting curve of nickel up to 100 GPa explored by XAS. *J. Geophys. Res. Solid Earth* **122**, 9921–9930 (2017).
35. R. Torchio et al., Melting curve and phase relations of Fe–Ni alloys: Implications for the Earth's core composition. *Geophys. Res. Lett.* **47**, 1–7 (2020).
36. A. Belonoshko et al., Stabilization of body-centred cubic iron under inner-core conditions. *Nat. Geosci.* **10**, 312–316 (2017).
37. Y. Lu et al., Premelting hcp to bcc transition in beryllium. *Phys. Rev. Lett.* **118**, 145702 (2017).
38. T. Sun, J. P. Brodholt, Y. Li, L. Vočadlo, Melting properties from ab initio free energy calculations: Iron at the Earth's inner-core boundary. *Phys. Rev. B.* **98**, 224301 (2018).
39. A. S. Côté, L. Vočadlo, J. P. Brodholt, Ab initio simulations of iron–nickel alloys at Earth's core conditions. *Earth Planet. Sci. Lett.* **345–348**, 126–130 (2012).
40. K. F. Kelton, A. L. Greer, Nucleation in Condensed Matter: Application in Materials and Biology (Elsevier, 2010).
41. M. W. Finnis, J. E. Sinclair, A simple empirical N-body potential for transition metals. *Philos. Mag. A* **50**, 45–55 (1984).
42. M. Ekholm, A. S. Mikhaylushkin, S. I. Simak, B. Johansson, I. A. Abrikosov, Configurational thermodynamics of Fe–Ni alloys at Earth's core conditions. *Earth Planet. Sci. Lett.* **308**, 90–96 (2011).
43. B. Martorell, J. Brodholt, I. G. Wood, L. Vočadlo, The effect of nickel on the properties of iron at the conditions of Earth's inner core: Ab initio calculations of seismic wave velocities of Fe-Ni alloys. *Earth Planet. Sci. Lett.* **365**, 143–151 (2013).
44. B. Zhang et al., Small-scale layered structures at the inner core boundary. *Nat. Commun.* **14**, 6362 (2023).
45. G. Pang et al., Enhanced inner core fine-scale heterogeneity towards Earth's centre. *Nature* **620**, 570–575 (2023).
46. T.-S. Phạm, H. Tkalčić, Up-to-fivefold reverberating waves through the Earth's center and distinctly anisotropic innermost inner core. *Nat. Commun.* **14**, 754 (2023).
47. G. Kresse, J. Furthmüller, Efficient iterative schemes for ab initio total-energy calculations using a plane-wave basis set. *Phys. Rev. B* **54**, 11169–11186 (1996).
48. N. D. Mermin, Thermal properties of the inhomogeneous electron gas. *Phys. Rev.* **137**, A1441 (1965).
49. R. M. Wentzcovitch, J. L. Martins, P. B. Allen, Energy versus free-energy conservation in first-principles molecular dynamics. *Phys. Rev. B* **45**, 11372–11374 (1992).
50. X. W. Fang, C. Z. Wang, Y. X. Yao, Z. J. Ding, K. M. Ho, Atomistic cluster alignment method for local order mining in liquids and glasses. *Phys. Rev. B* **82**, 184204 (2010).
51. Y. Sun et al., 'Crystal genes' in metallic liquids and glasses. *Sci. Rep.* **6**, 23734 (2016).
52. W. M. Brown, P. Wang, S. J. Plimpton, A. N. Tharrington, Implementing molecular dynamics on hybrid high performance computers-short range forces. *Comput. Phys. Commun.* **182**, 898–911 (2011).
53. J. R. Morris, C. Z. Wang, K. M. Ho, C. T. Chan, Melting line of aluminum from simulations of coexisting phases. *Phys. Rev. B* **49**, 3109–3115 (1994).
54. S. Nosé, A unified formulation of the constant temperature molecular dynamics methods. *J. Chem. Phys.* **81**, 511 (1984).

Supplementary Information for

Unveiling the effect of Ni on the formation and structure of Earth's inner core

Yang Sun[1,2,3], Mikhail I. Mendelev[3], Feng Zhang[3], Xun Liu[4], Bo Da[4], Cai-Zhuang Wang[3], Renata M. Wentzcovitch[2,5-8] and Kai-Ming Ho[3]

[1]*Department of Physics, Xiamen University, Xiamen 361005, China*
[2]*Department of Applied Physics and Applied Mathematics, Columbia University, New York, NY 10027, USA*
[3]*Department of Physics, Iowa State University, Ames, IA 50011, USA*
[4]*Research and Services Division of Materials Data and Integrated System, National Institute for Materials Science, Ibaraki 305-0044, Japan*
[5]*Department of Earth and Environmental Sciences, Columbia University, New York, NY 10027, USA*
[6]*Lamont–Doherty Earth Observatory, Columbia University, Palisades, NY 10964, USA*
[7]*Data Science Institute, Columbia University, New York, NY 10027, USA*
[8]*Center for Computational Quantum Physics, Flatiron Institute, New York, NY 10010, USA*

*Corresponding Authors: Yang Sun; Mikhail I. Mendelev; Renata M. Wentzcovitch
Email: yangsun@xmu.edu.cn mikhail.mendelev@gmail.com rmw2150@columbia.edu

This PDF file includes:

> Supplementary text
> Figures S1 to S4
> Tables S1 to S2
> SI References

Supplementary Text

This supplementary information contains details of semi-empirical potential development in Note S1 and the cooling simulation in calculation of the kinetic prefactor in Note S2.

Note S1. Potential development of semi-empirical potential for Ni

Several target properties were used to develop Ni's embedded atom method (EAM) potential. The first group consisted of basic fcc Ni properties at T=0 and P=0 listed in Table S1, including lattice parameter, cohesive energy, unrelaxed vacancy formation energy, and elastic constants, C_{ij}. This is a standard set routinely used in development procedures for semi-empirical potentials. Since the condition of T=0 and P=0 is very far from the high *PT* conditions we were interested in, these properties were fitted with low weights. The examination of Table S1 shows that the developed potential reproduces these properties reasonably well (obviously, the semi-empirical potentials explicitly fitted to these conditions provide much better reproduction of these properties).

Next, we chose an fcc lattice parameter that would approximately give p=323 GPa at T=5800 K, which was our initial guess for the fcc melting temperature. This was done by manually adjusting the fcc lattice parameters at these conditions. The accuracy of such a procedure was not very high such that we ended up with the lattice parameter, which gave the pressure of 330 GPa. That was not a problem with our fitting procedure since, in reality, the potential was fitted not to the lattice parameters but to the pressure corresponding to the given lattice parameters. This pressure was determined from the AIMD simulation with sufficient accuracy.

Two types of deformation were applied to the fcc model to get non-zero ε_{xx} and ε_{yz} (the absolute values of ε were 0.01). The stress tensor components were determined from the AIMD simulation for each case. The differences between these stress tensor components and the components of the stress tensors of the corresponding initial models divided by the deformation value were defined as the elastic responses, R_{ij}. R_{ij} would be the same as the related elastic constants if all components of the stress tensor of the initial model were zero. R_{ij} constants reflect the crystal response to the applied deformation, and fitting these constants should warrant reproducing the correct elastic properties of the considered phases. The obtained AIMD values are presented in Table S2, showing that the developed potential reasonably reproduces the elastic responses obtained from the AIMD simulation.

Since we were interested in determining the melting temperature, it was desirable to have the liquid structure obtained with the EAM potential as close as possible to the AIMD liquid structure. Therefore, it was essential to include the liquid density and structure data obtained from the AIMD simulation in the potential development procedure. The method to achieve this is described in (1). Figure S1 shows the pair correlation functions of liquid Ni obtained from the AIMD and classical MD simulations at Earth's core conditions utilizing the developed EAM potential. It indicates that the liquid structure from developed potential agrees well with the AIMD data.

Using the solid-liquid coexistence approach (2) with 22,500 atoms, the melting temperatures of Ni phases are predicted by the EAM potential, which is 6728 K for bcc, 6543 K for hcp, and 6588 K for fcc at 323 GPa. These data provide the references for the thermodynamic integration to compute the *ab initio* melting temperatures. In addition, the melting temperature of fcc at 100 GPa is predicted as 3975 K by the EAM potential. Previous experiments at 100 GPa reported the melting temperature of 3736 K with an error bar ~300 K (3) and 3699 at 100GPa with an error bar ~100 K (4).Therefore the present EAM potential provides a consistent estimation of Ni's T_m with experiments.
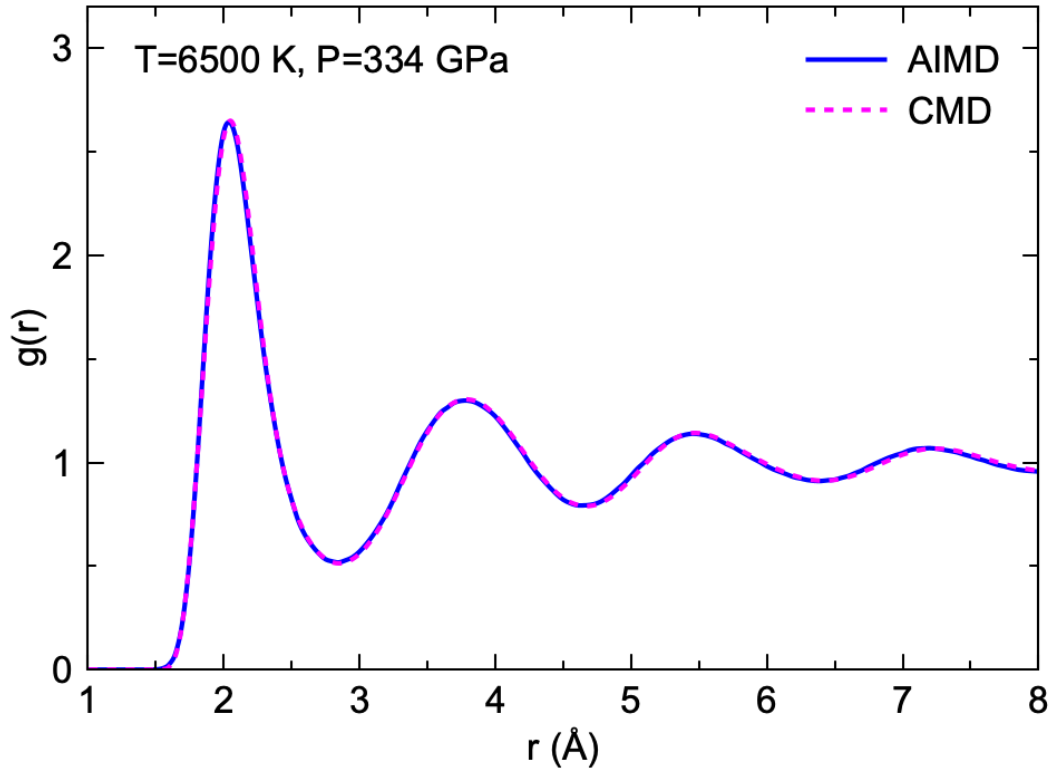

Fig. S1. Pair correlation functions of liquid Ni under the Earth's core conditions obtained from the AIMD and classical MD simulations with the developed EAM potential.

Supplementary Note 2 | Cooling simulation for Fe, Fe₉₅Ni₅ and Fe₈₅Ni₁₅ melts.

In Fig. S2, we provide additional MD simulations of the cooling process with 108,000 atoms to examine the Ni effect on Fe's crystallization. The Fe, Fe₉₅Ni₅ and Fe₈₅Ni₁₅ melts are cooled from ΔT=-900 K to -2900 K within 20 ns, corresponding to a cooling rate of 10^{11} K/s. Due to the stochastic nature of crystallization, we performed four independent simulations under 323 GPa. One can see that the Fe₈₅Ni₁₅ melts solidified at ~1300 K supercooling, Fe₉₅Ni₅ melts solidified at ~1600 K supercooling, while Fe melts solidified at ~1700 K. 15% Ni reduces the required supercooling by 400 K. Therefore, Ni indeed has a strong effect on the Fe's crystallization under core conditions.
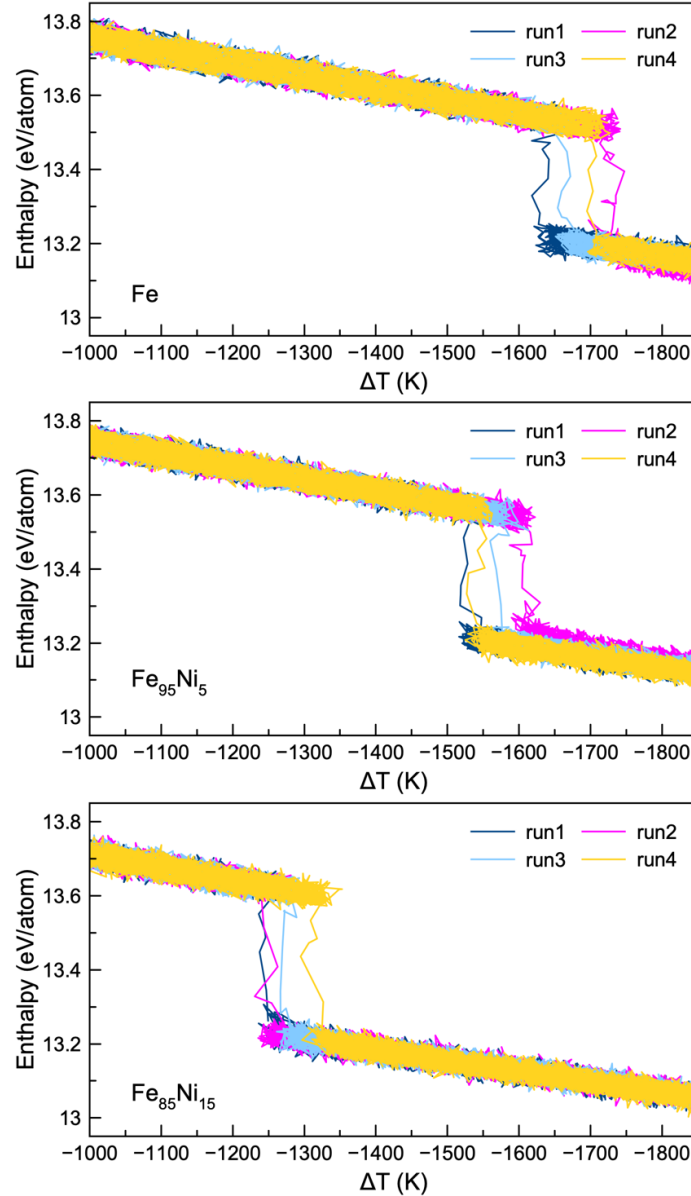

Fig. S2. The enthalpy as a function of supercooling temperature from the continuous cooling of Fe, Fe₉₅Ni₅, and Fe₈₅Ni₁₅ melts at P=323GPa. Each simulation is independently performed four times. The supercooling is referenced to the melting temperature of Fe's hcp phase, as $\Delta T = T - T_m^{hcp}$.
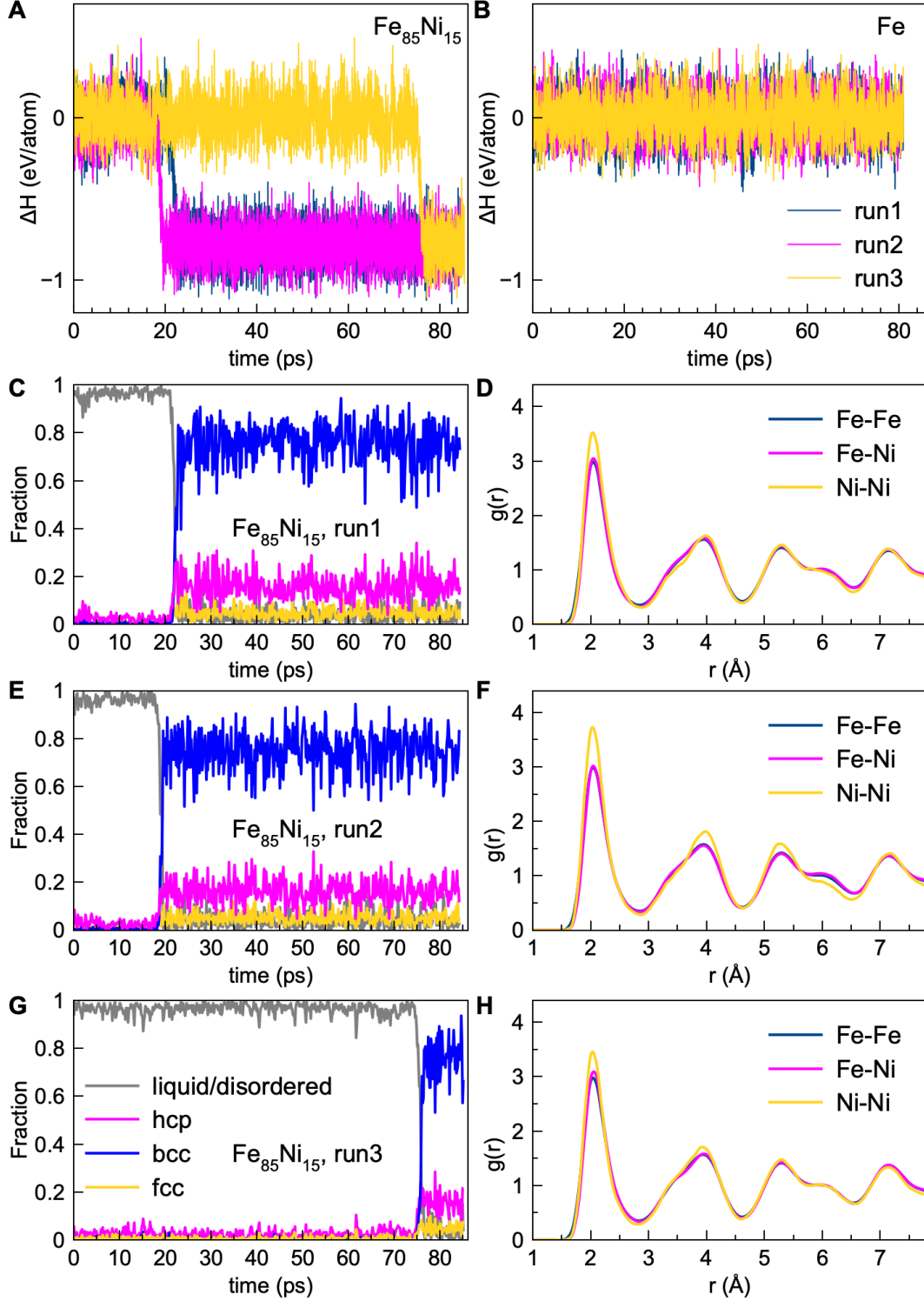
Fig. S3. Additional three simulations of Fe₈₅Ni₁₅ and Fe liquid at 310 GPa and 5000 K. (*A*) The enthalpy change as a function of simulation time for Fe₈₅Ni₁₅. (*B*) The enthalpy change for Fe. (*C,E,G*) The fraction of liquid/disordered and crystalline atoms with fcc, bcc, and hcp coordinations as a function of time, respectively. (*E,F,G*) The respective partial pair correlation functions of the crystallized Fe₈₅Ni₁₅ phase in three runs.
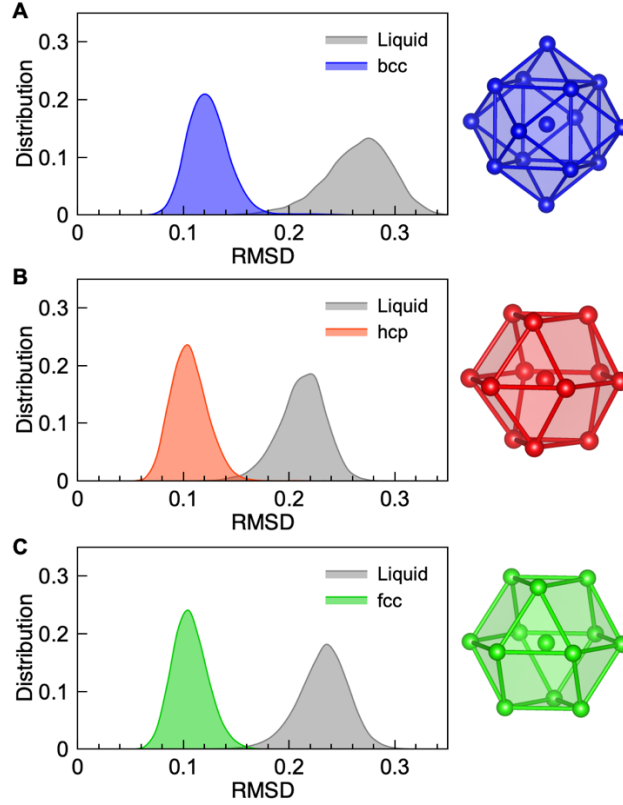
Fig. S4. Structural order parameter to distinguish bcc, hcp, and fcc from liquid for Ni at 323 GPa and 6000 K. (*A*) Root mean square deviation (RMSD) to perfect bcc cluster between the bulk liquid and bcc phase. (*B*) RMSD between liquid and hcp. (*C*) RMSD between liquid and FCC. The right panels show the perfect bcc, hcp, and fcc clusters, respectively.

Table S1. Ni fcc properties at T=0 and p=0.

Property	Target value	EAM potential
Lattice parameter (Å)	3.517	3.518
Cohesive energy (eV/atom)	-4.45	-4.840
Unrelaxed vacancy formation energy (eV/atom)	1.5	1.47
C_{11} (GPa)	247	252
C_{12} (GPa)	147	162
C_{44} (GPa)	125	96

Table S2. The elastic response.

Elastic response tensor components (GPa)	AIMD	EAM
R_{11}	1329	1316
R_{12}	1204	1248
R_{44}	449	421

SI References

1. M. I. Mendelev, D. J. Srolovitz, Determination of alloy interatomic potentials from liquid-state diffraction data. *Phys. Rev. B* **66**, 014205 (2002).

2. J. R. Morris, C. Z. Wang, K. M. Ho, C. T. Chan, Melting line of aluminum from simulations of coexisting phases. *Phys. Rev. B* **49**, 3109–3115 (1994).

3. S. Boccato, *et al.*, The Melting Curve of Nickel Up to 100 GPa Explored by XAS. *J. Geophys. Res. Solid Earth* **122**, 9921–9930 (2017).

4. O. T. Lord, *et al.*, The melting curve of Ni to 1 Mbar. *Earth Planet. Sci. Lett.* **408**, 226–236 (2014).